Chaotic dynamics of large-scale structures in a turbulent wake

Eliott Varon,[1,2,*] Yoann Eulalie,[3] Stephie Edwige,[3] Philippe Gilotte,[3] and Jean-Luc Aider[1,2,†]
[1]*Laboratoire PMMH, CNRS UMR7636, ESPCI Paris, PSL Research University, 10 rue Vauquelin, Paris, France*
[2]*Laboratoire PMMH, CNRS UMR7636, Université Pierre et Marie Curie, 10 rue Vauquelin, Paris, France*
[3]*Plastic Omnium Auto Extérieur Services (POAES), Parc Industriel de la Plaine de l'Ain, Sainte-Julie, France*
(Received 26 July 2016; published 17 March 2017)

The dynamics of a three-dimensional (3D) bimodal turbulent wake downstream of a square-back Ahmed body are experimentally studied in a wind tunnel through high-frequency wall-pressure probes mapping the rear of the model and a horizontal two-dimensional (2D) velocity field. The barycenters of the pressure distribution over the rear part of the model and the intensity recirculation are found highly correlated. Both described the most energetic large-scale structures dynamics, confirming the relation between the large-scale recirculation bubble and its wall-pressure footprint. Focusing on the pressure, its barycenter trajectory has a stochastic behavior but its low-frequency dynamics exhibit the same characteristics as a weak strange chaotic attractor system, with two well-defined attractors. The low-frequency dynamics associated to the large-scale structures are then analyzed. The largest Lyapunov exponent is first estimated, leading to a low positive value characteristic of strange attractors and weak chaotic systems. Afterwards, analyzing the autocorrelation function of the timeseries, we compute the correlation dimension, larger than two. The signal is finally transformed and analyzed as a telegraph signal, showing that its dynamics correspond to a quasirandom telegraph signal. This is the first demonstration that the low-frequency dynamics of a turbulent 3D wake are not a purely stochastic process but rather a weak chaotic process exhibiting strange attractors. From the flow control point of view, it also opens the path to more simple closed-loop flow-control strategies aiming at the stabilization of the wake and the control of the dynamics of the wake barycenter.

DOI: 10.1103/PhysRevFluids.2.034604

I. INTRODUCTION

It is well known that the turbulent wakes downstream of three-dimensional (3D) bluff bodies can be very complex, exhibiting large-scale and small-scale coherent structures with strongly intermittent behaviors. Among the various 3D bluff bodies, one of the most famous is the so-called Ahmed body, which is a model used in automotive aerodynamics to study the wake of a very simplified passenger car [1]. Depending on the geometry of the rear part, the overall structure of the wake changes together with the aerodynamic drag coefficient. One can find a competition between large-scale streamwise longitudinal vortices [2], spanwise Kelvin-Helmholtz vortices, recirculation bubbles, or toroïdal vortices. If the time-averaged velocity fields are relatively simple and well defined, the instantaneous velocity fields are very complex and exhibit together large- and small-scale structures, leading to one of the most complex 3D turbulent flows. Recently, it has been shown experimentally [3] and numerically [4] that a square-back Ahmed body at high Reynolds numbers exhibits a peculiar behavior with a bimodal wake, which was first observed in the laminar regime [5]. Indeed, depending on the geometric parameters (aspect ratio of the bluff body's cross section [6] and underbody flow [7]), one can observe a right-left oscillation of the global wake, defining the so-called reflectional symmetry-breaking (RSB) modes.

*eliott.varon@espci.fr
†jean-luc.aider@espci.fr; https://blog.espci.fr/jlaider/

The large-scale dynamics of another wake, which is 3D turbulent axisymmetric, has been captured in Ref. [8], using a deterministic model for the persistent laminar instabilities coupled with a stochastic representation of the turbulent fluctuations. For such dynamics, two different time scales are notable: A short one is associated to the vortex shedding process whereas the symmetry-breaking one is characterized by a long time scale [3,9]. We are interested here in the characterization of the bimodal oscillation of the near wake in the framework of dynamical systems theory and, more precisely, as a chaotic system.

A classic example of a chaotic system is the Lorenz attractor and corresponding Lorenz system, whose characteristic butterfly shape is famous [10]. The so-called Lorenz system is a simplified weather model defined by the set of three ordinary differential equations:

$$\begin{aligned} \dot{x} &= \sigma(y - x), \\ \dot{y} &= x(R - z) - y, \\ \dot{z} &= xy - \beta z. \end{aligned} \tag{1}$$

With the correct choice for the three parameters ($\sigma = 16$, $R = 45.92$, and $\beta = 4$), the trajectory plotted in the (x,y,z) space exhibits a chaotic behavior, circling in an apparent random manner between two stable attractors.

Since the pioneering work of Lorenz, it has been shown that many biological, natural, or artificial systems, either at very small or very large scales, follow a chaotic dynamics. The brain wave activity (EEG) [11] or the heart rate activity (ECG) [12] can exhibit chaotic behaviors. In some cases, chaotic excitations can be used to study the response of mechanical systems. A variation in correlation dimensions can be used as an indicator of a fracture in the overall structure [13]. Chaotic behavior has been found in trading market time series [14]. One can also find chaotic behavior for large-scale phenomena like earthquakes [15].

In the following, we will first show how the 3D full turbulent wake dynamics can be characterized by the single trajectory of its projected barycenter. After recovering the classic chaotic pattern, we will analyze more thoroughly the inner characteristics of the large-scale dynamical system. We will, in particular, evaluate the family of random process to which it belongs, the largest Lyapunov exponent of the system and the correlation dimension.

II. EXPERIMENTAL SETUP

A. Ahmed body

The bluff body is a 0.7 scale of the original Ahmed body ($L = 0.731$ m long, $H = 0.202$ m high, and $W = 0.272$ m wide), as described in Ref. [16]. The rear part of the model is a square-back geometry with sharp edges.

B. Wind tunnel

Experiments are carried out in the PRISME laboratory wind tunnel (Orléans, France). The model is mounted on a raised floor with a properly profiled leading edge and an adjustable trailing edge to avoid undesired flow separations. The ground clearance is set to $C = 5$ cm. In the following, the free-stream velocity is $U_\infty = 30$ m s^{-1}, which corresponds to a Reynolds number based on the height of the model $\mathrm{Re}_H = U_\infty H/\nu_{\mathrm{air}} = 3.9\times10^5$, where ν_{air} is the kinematic viscosity of the air at ambient temperature. The origin is located on the rear of model ($x = 0$), in the vertical symmetry plane ($y = 0$) and on the raised floor ($z = 0$). Nondimensionalization is applied to distances such as $x^* = x/H$, $y^* = y/H$, and $z^* = z/H$.

C. Sensors

The wall pressure over the rear part of the model is studied using a set of 95 pressure vinyls defining an area denoted S_p and covering 70% of the entire surface S_r, as shown in Fig. 1. Each vinyl is 2 cm away from each of its neighbors and is connected to a 32-channel microDAQ pressure scanner,

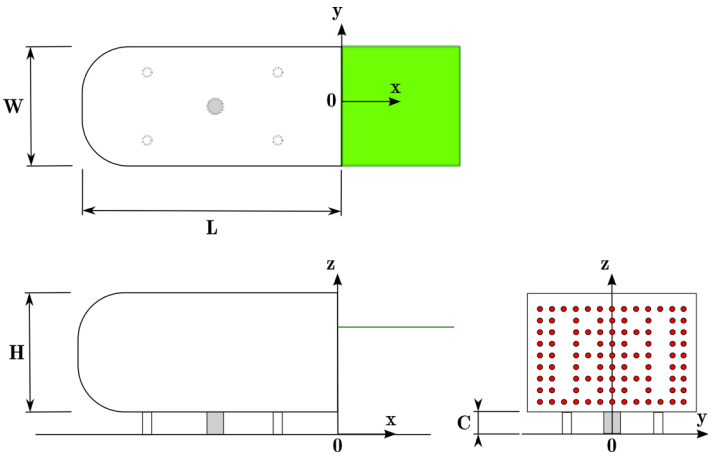

FIG. 1. Upper view (top figure) and side view (lower left figure) and view from behind (lower right figure) of the Ahmed body. The PIV measurement plane is shown on top (green rectangle) and lower left (green line) figure. The rear part of the model is mapped with 95 pressure sensors (red circles on lower right figure). The bluff body is fixed on the aerodynamic balance through a supplementary leg (gray part on lower figures).

ensuring an accuracy of ± 17 Pa located inside the body. The number of samples per acquisition is unfortunately bounded to $N = 3\times10^4$, making the sampling frequency for the pressure f_P dependent on the acquisition time T_P: $f_P = N/T_P$. A typical instantaneous pressure field is shown in Fig. 2(a). From these instantaneous pressure fields, a global indicator of the state of the wake can be inferred, as will be detailed in the following section.

The velocity fields are obtained using a standard particle image velocimetry (PIV) setup based on a double-frame 14.50-Hz TSI camera streaming snapshots on a computer and synchronized with a double-cavity pulsed YaG laser. The investigated PIV plane is the near wake horizontal plane at $z^* = 1$.

The two-dimensional (2D) velocity fields are computed at the frequency $f_{\mathrm{PIV}} = 4$ Hz using an optical flow algorithm implemented on a graphics processing unit. The interrogation window size is 16×16 pixels and the calculation is based on three iterations for each of the three pyramid

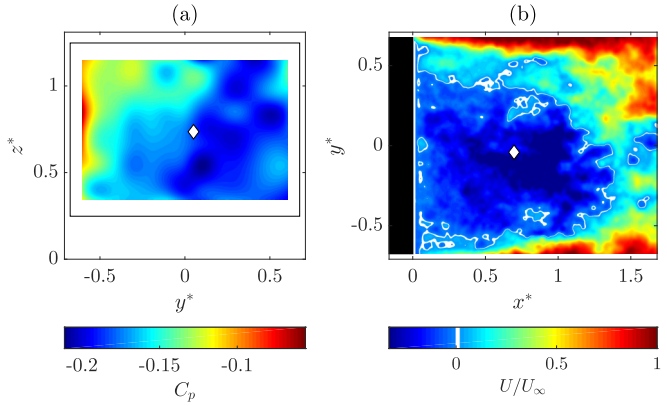

FIG. 2. Typical (a) instantaneous pressure field over the rear part of the model and (b) instantaneous 2D velocity field in the horizontal plane shown in Fig. 1. The diamond (white) is the instantaneous barycenter position of respectively (a) the rear pressure G_p and (b) the intensity recirculation G_{rec}, which are introduced and discussed in the following section.

reduction levels. One can find more details on this measurement method in Refs. [17–21], which rigorously demonstrate its offline accuracy as well as its online efficiency in closed-loop flow control experiments. An example of a 2D instantaneous velocity field is shown in Fig. 2(b). One can see the complexity of the turbulent wake, with large- and small-scale strongly fluctuating vortices.

The bluff body is linked to an aerodynamic balance through a cylindrical leg of diameter 32 mm localized at the center of the bottom face. This leg does not modify the reflectional symmetry of the square-back body but it has certainly an influence on the near wake, which is discussed in the following section. The aerodynamic data are not used in the present study.

III. DYNAMIC OF THE WAKE BARYCENTER

A. Wake characterization

We are interested in the large-scale dynamics of the global wake. This is the reason why we define the instantaneous wall-pressure barycenter, which can be seen as the footprint of the wake. Denoting the space average of a quantity f over an area S as $\langle f \rangle_S$, we compute the pressure barycenter at $x^* = 0$ as

$$\overrightarrow{OG_p(t)} = \begin{pmatrix} y_p^*(t) \\ z_p^*(t) \end{pmatrix} = \begin{pmatrix} \frac{\langle y^* p(t) \rangle_{S_p}}{\langle p(t) \rangle_{S_p}} \\ \frac{\langle z^* p(t) \rangle_{S_p}}{\langle p(t) \rangle_{S_p}} \end{pmatrix}, \tag{2}$$

where $p(t) = p(y^*, z^*, t)$ is the local pressure measured at time t. Thus the instantaneous barycenter of the depression can be tracked at each time step. In the same way, we define the instantaneous recirculation intensity barycenter from the velocity fields in the PIV horizontal plane at $z^* = 1$ as

$$\overrightarrow{OG_{\text{rec}}(t)} = \begin{pmatrix} x_{\text{rec}}^*(t) \\ y_{\text{rec}}^*(t) \end{pmatrix} = \begin{pmatrix} \frac{\langle x^* u_{\text{rec}}(t) \rangle_{A_{\text{rec}}(t)}}{\langle u_{\text{rec}}(t) \rangle_{A_{\text{rec}}(t)}} \\ \frac{\langle y^* u_{\text{rec}}(t) \rangle_{A_{\text{rec}}(t)}}{\langle u_{\text{rec}}(t) \rangle_{A_{\text{rec}}(t)}} \end{pmatrix}, \tag{3}$$

where $u_{\text{rec}}(t) = u_{\text{rec}}(x^*, y^*, t)$ and $A_{\text{rec}}(t)$ are respectively the local streamwise component of the recirculation velocity and the recirculation area at time t. An example of the evolution in time is given for y_p^* [Fig. 3(a)] and y_{rec}^* [Fig. 3(c)].

The probability density function (PDF) is then computed from the spanwise position of both barycenters. Figure 3 shows clearly the bimodal behavior of the turbulent wake, whether it is through the pressure barycenter PDF $P_{y_p^*}$ [Fig. 3(b)] or the recirculation barycenter PDF $P_{y_{\text{rec}}^*}$ [Fig. 3(d)]. Indeed their PDFs have two peaks whose positions are nearly symmetric with respect to the y axis. The difference in the peaks value is due to the low acquisition time as observed in Ref. [7]. Longer acquisitions only done for the pressure show well two peaks of the same level. The small amount of data regarding the PIV explains the noisy aspect of $P_{y_{\text{rec}}^*}$. The two identified RSB modes are the ($y_p^* < 0$, $y_{\text{rec}}^* > 0$) state and the ($y_p^* > 0$, $y_{\text{rec}}^* < 0$) state.

Even if the barycenters seem to switch successively from a mode to the other randomly, some characteristic time scales and characteristic frequencies can be estimated. The mean time spent in each mode is $T_{\text{RSB}} = 1.57 \pm 0.32$ s. The estimated switching frequency is $f_{\text{switch}} = 0.56 \pm 0.08$ Hz, whereas the switch itself lasts for $T_{\text{switch}} = 0.30 \pm 0.05$ s. As expected, these results have a high dispersion: Their respective standard deviations are $\sigma_{T_{\text{RSB}}} = 2.1 \pm 0.3$ s and $\sigma_{T_{\text{switch}}} = 0.11 \pm 0.01$ s.

Regarding the normal to the wall position z_p^* and the streamwise position x_{rec}^* presented for the pressure [Figs. 4(a) and 4(b)] and the recirculation intensity respectively [Figs. 4(c) and 4(d)], these positions are stable. Indeed, their respective PDF, $P_{z_p^*}$ and $P_{x_{\text{rec}}^*}$, show only one mode.

Thus the same lateral symmetry-breaking mechanism is observed in our wake topology as the ones presented without a central leg in Refs. [3,7]. The effects of the modified ground clearance on the wake reversal behind a square-back bluff body have been studied in Ref. [22]. It was reported in particular that the presence of a circular cylinder, very similar to the central leg attached to the aerodynamical balance in our experiments, changes only the mode position for z_p^* but does not cancel the lateral bimodality.

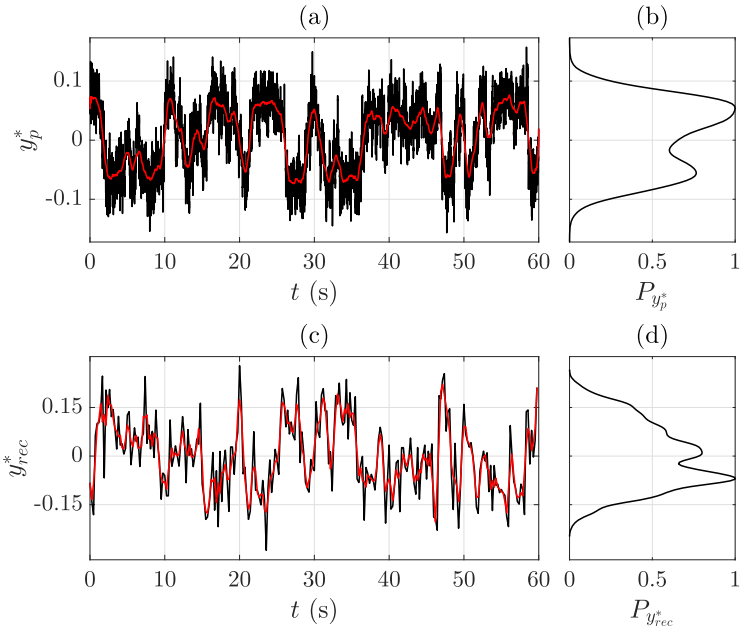

FIG. 3. Pressure barycenter spanwise position y_P^*: (a) evolution in time and (b) normalized PDF $P_{y_P^*}$ for $T_P = 1$ min ($f_P = 500$ Hz). Recirculation intensity barycenter spanwise position y_{rec}^*: (c) evolution in time and (d) normalized PDF $P_{y_{\text{rec}}^*}$ for $T_{\text{PIV}} = 1$ min. Red curves show the data smoothed over 1 s.

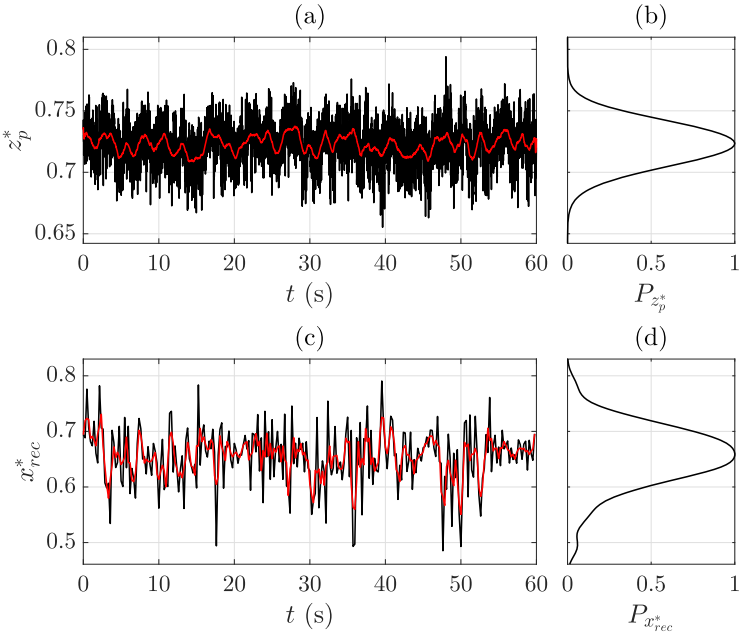

FIG. 4. Pressure barycenter spanwise position z_P^*: (a) evolution in time and (b) normalized PDF $P_{z_P^*}$ for $T_P = 1$ min ($f_P = 500$ Hz). Recirculation intensity barycenter spanwise position x_{rec}^*: (c) evolution in time and (d) normalized PDF $P_{x_{\text{rec}}^*}$ for $T_{\text{PIV}} = 1$ min. Red curves show the data smoothed over 1 s.

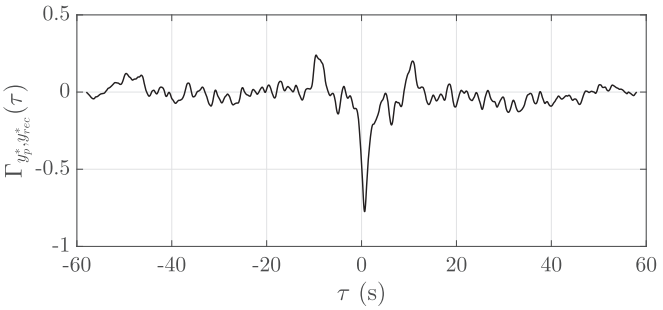

FIG. 5. Normalized cross correlation of y_P^* and y_{rec}^*.

The relation between the dynamics of the wake, characterized by its instantaneous recirculation area, and the dynamics wall pressure is not straightforward because of the complex 3D flow. To study their relationship, the normalized cross correlation of y_P^* and y_{rec}^* has been computed for five 1-min runs: $\Gamma_{y_p^*,y_{\text{rec}}^*}(\tau) = y_p^*(\tau) \otimes y_{\text{rec}}^*(\tau)$. The results show a strong correlation and an almost nonexistent delay between the two measurements as illustrated by Fig. 5.

The value of the peak is $\Gamma_{y_p^*,y_{\text{rec}}^*}(\tau \sim 0) = -0.84 \pm 0.05$ so both barycenters are in phase opposition. When the depression is located in the negative part of the rear surface ($y_p^* < 0$), the recirculation bubble is located in the positive one ($y_{\text{rec}}^* > 0$) and vice versa. This behavior was first observed in Ref. [23]. So the wake states can be characterized either by the pressure barycenter or by the recirculation intensity one. In the following, we present only results regarding y_p^* for several independent experiments of various lengths $T_P = \{2; 5 \text{ min}\}$ acquisition runs ($f_P = 250$ Hz and $f_P = 100$ Hz respectively).

B. Coherent structures

As we are interested in the dynamics of the large-scale structures, we analyze the spatiotemporal organization of the wall-pressure spatial distributions using the proper orthogonal decomposition (POD). It is an efficient approach to detect coherent structures in turbulent flows [24,25]. Thus we apply the POD on the rear pressure coefficient fluctuations $\tilde{C_p}$:

$$\tilde{C_p}(t) \sim \sum_{i=1}^{k} a_i(t)\Phi_i, \tag{4}$$

where k is the number of POD modes Φ_i carrying most of the coherent structures energy and a_i are the corresponding temporal coefficients. The energy distribution of the first 25 POD modes is given in Fig. 6, showing that the first five modes contain 75% of the total energy.

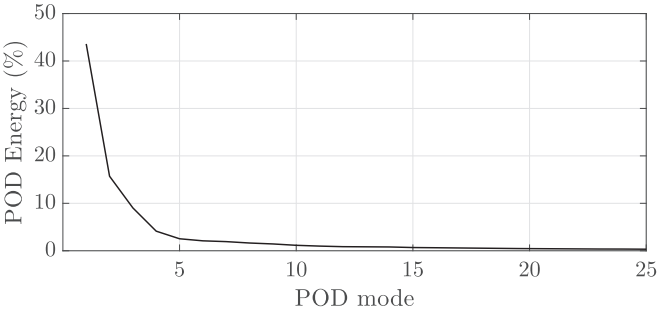

FIG. 6. Energy distribution of the first 25 POD modes of the rear pressure.

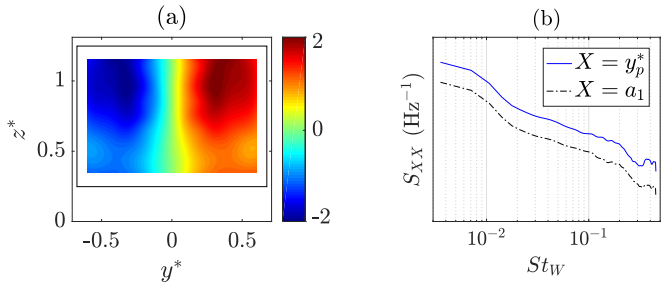

FIG. 7. (a) First POD mode Φ_1 (43%) and (b) PSD of its corresponding coefficient a_1 (dashed black line) together with the PSD of y_p^* (solid blue line).

The power spectral density (PSD) is computed to analyze the dynamics of the first POD modes. For practical comparisons we express the frequency f as the Strouhal number based on the width bluff body: $\mathrm{St}_W = fW/U_\infty$.

The most remarkable results are that the first mode Φ_1 represents 43% of the total energy and that its spatial organization exhibits the global symmetry breaking presented on Fig. 7(a). Moreover, its spectral signature is identical to the one of the pressure barycenter, displayed in Fig. 7(b): The low frequencies, $\mathrm{St}_W < 0.02$, contain most of the power spectrum. Thus the pressure barycenter is a direct measure of the most energetic large-scale coherent structure governed by a long time scale.

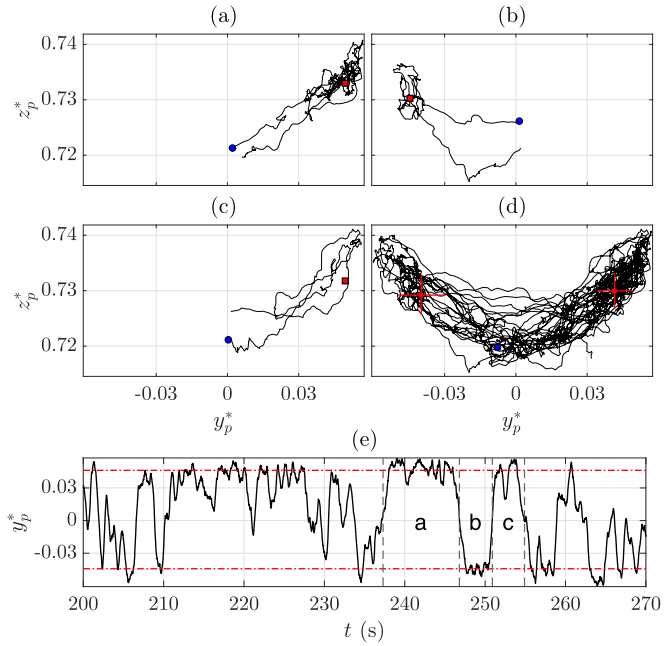

FIG. 8. Evolution in space of the pressure barycenter G_P (black line for the trajectory and blue circle for the last position) with the identified centers (red squares) for three successive small intervals: (a) $t \in [237; 247]$, (b) $t \in [247; 251]$, (c) $t \in [251; 255]$, and (d) a larger interval $t \in [237; 266]$ (red cross for the standard deviation). (e) $y_p^*(t)$ for $t \in [200; 270]$ with the spanwise position of the two centers (dash-dotted red lines). All intervals are in seconds and data are smoothed for clarity. See Supplemental Material [26].

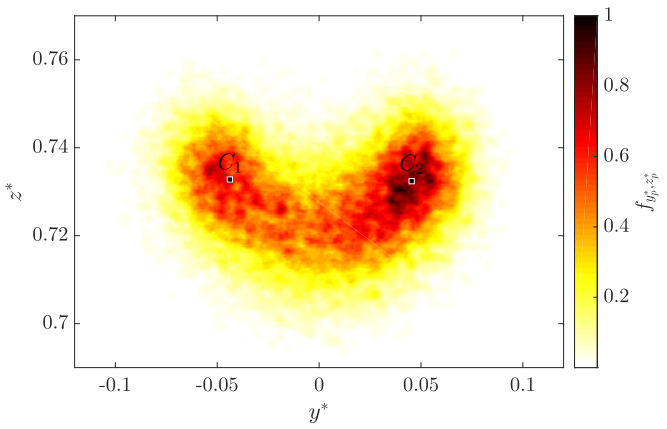

FIG. 9. Normalized 2D PDF of the pressure barycenter G_P with the two identified local maxima of the PDF (black squares).

C. Quasistrange attractor dynamics

The positions of the pressure barycenter G_P for three successive stays in the RSB modes are displayed in Figs. 8(a)–8(c). We also plot the most probable position (red square) near which G_p evolves during each stay.

Figures 8(d) and 8(e) show longer tracking with the most probable positions of each RSB mode, disclosing two y-axis symmetric points which acts like the centers of a strange attractor.

The 2D PDF of the pressure barycenter is computed to analyze its most frequent positions on the rear. We also calculate the positions of the identified centers, denoted $C_1(y^*_{C_1},z^*_{C_1})$ and $C_2(y^*_{C_2},z^*_{C_2})$, as local modes of the PDF $P_{y^*_p}$, such as

$$\overrightarrow{OC_1} = \begin{pmatrix} y^*_{p_{|\max_{y^*_p<0} P_{y^*_p}}} \\ z^*_{p_{|\max_{y^*_p<0} P_{y^*_p}}} \end{pmatrix} \quad \text{and} \quad \overrightarrow{OC_2} = \begin{pmatrix} y^*_{p_{|\max_{y^*_p>0} P_{y^*_p}}} \\ z^*_{p_{|\max_{y^*_p>0} P_{y^*_p}}} \end{pmatrix}. \tag{5}$$

The results, shown in Fig. 9, reveal two areas highly preferred by the barycenter, corresponding to the two RSB states. For each area, a quasiattractive center can be identified, such as $y^*_{C_1} \sim -y^*_{C_2}$ and $z^*_{C_1} \sim z^*_{C_1}$. During the switch between these two positions, the pressure barycenter follows preferentially a trajectory along a well-defined path. In the following section we characterize the signal y^*_p.

IV. CHARACTERIZATION OF THE ATTRACTOR

A. Structure function

Analyzing the signal to know whether the dynamics of the wake are chaotic or stochastic is of prime interest. An effective approach is to study its self-affinity by computing its first-order ($k = 1$) [27] or its second-order ($k = 2$) [28] structure function S_k, defined as

$$S_k(n) = \langle |y^*_p(i+n) - y^*_p(i)|^k \rangle_i, \tag{6}$$

where n is the lag and $\langle . \rangle_i$ stands for the average over $N - n$ points. According to Ref. [29], if y^*_p is fractal, S_k follows a scaling law for small n:

$$S_k(n) \propto n^{kh}, \tag{7}$$

where h is the so-called scaling exponent. If the signal X is chaotic, then $h = 1$. If it is stochastic, then its power spectrum follows a power-law $S_{XX}(\mathrm{St}_W) \propto \mathrm{St}_W^{-\alpha}$ and $\alpha = 2h + 1$. However, S_k alone

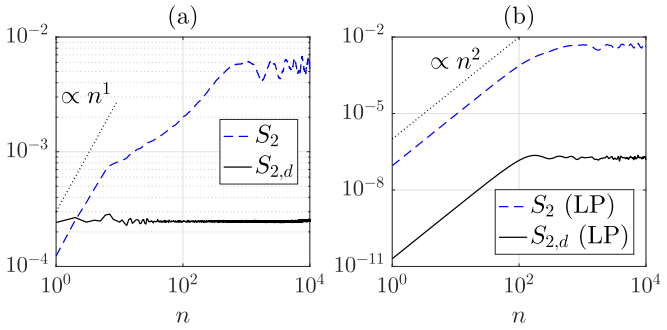

FIG. 10. (a) Second-order structure functions of y_p^* (dashed blue line) and of its first derivative (solid black line). (b) Second-order structure functions of the LP filtered y_p^* (dashed blue line) and of its first derivative (solid black line). $f_p = 250$ Hz.

is not enough to conclude and the structure function of the first derivative of the signal y_p^*, denoted as $S_{k,d}$, needs to be computed [28]. Thus, if it is stochastic then $S_{k,d}$ is almost constant, and if the signal is chaotic then $S_{k,d}(n)$ follows a scaling law for small n. Figure 10 displays S_2 and $S_{2,d}$ for the raw signal y_p^* (a) and for the signal on which we apply a low-pass (LP) filter (b) to only select low-frequency modes which have the highest magnitudes: $\mathrm{St}_W < 10^{-3}$ [see Fig. 7(b)].

The raw signal behaves clearly like a fractal noise with $h = 1/2$ implying $\alpha = 2$, which is in agreement with Refs. [3,30]. Conversely the LP filtered data appear to be chaotic since $h = 1$ and $S_{2,d}$ is not constant. It is noteworthy that the same observations hold for $k = 1$.

B. Embedding dimension

As we only observe a part of the nonlinear wake dynamics (rear body pressure and 2D-2Components velocity fields of the near wake), we cannot experimentally access to its complete phase space. But Refs. [31,32] provide the so-called embedding methods to reconstruct a pseudophase space from time series. Thus, according to the pioneering Takens's time-delay embedding method [33], we build the M state vectors $\{Y_i\}_{i=1\ldots M}$:

$$Y_i(m) = \{y_p^*(i) y_p^*(i+J) \ldots \; y_p^*[i+(m-1)J]\}, \tag{8}$$

where m is the embedding dimension and J is the reconstruction delay, implying $M = N - (m-1)J$. J is computed trough the mutual information process [34] using improved kernel density estimation algorithm [35,36] to avoid *redundance* (J too small) and *irrelevance* (J too large) in phase space reconstruction [37]. We then determine the minimum value of m from y_p^*, following Cao's method [38], which is based on the false nearest neighbor algorithm of Ref. [39]. It should be noted that the values obtained for J are also checked through improved Celluci's algorithm [40,41].

Cao's method is summarized here since it enables us also to distinguish deterministic and stochastic time series. The idea is to evaluate how the mean distance between close state vectors $E(m)$ evolves with respect to m. Over the real embedding dimension $E(m)$ does not change anymore. We look for the closest neighbor $Y_{\mathcal{N}(i,m)}(m)$ of each state vector $Y_i(m)$:

$$\min_{\mathcal{N}(i,m)\neq i} \|Y_i(m) - Y_{\mathcal{N}(i,m)}(m)\|, \quad i \in [\![1; M]\!], \tag{9}$$

where $\|.\|$ stands for the Euclidean distance. The ratio of the distances in m and $m+1$ dimensions for Y_i is

$$a_{i,m} = \frac{\|Y_i(m+1) - Y_{\mathcal{N}(i,m)}(m+1)\|}{\|Y_i(m) - Y_{\mathcal{N}(i,m)}(m)\|}. \tag{10}$$

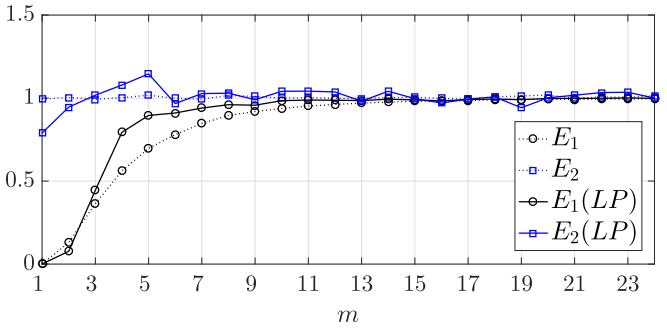

FIG. 11. $E_1(m)$ (black circle) and $E_2(m)$ (blue square) computed from raw (dashed line) and LP filtered (solid line) signal y_p^*. $f_p = 100$ Hz. The large-scale dynamics associated with the LP filtered signal show a chaotic signature.

Finally $E(m)$ is computed:

$$E(m) = \frac{1}{M}\sum_i a_{i,m}. \tag{11}$$

For convenience, its evolution is evaluated through $E_1(m)$,

$$E_1(m) = \frac{E(m+1)}{E(m)}, \tag{12}$$

and if $\exists m \backslash \forall k \geqslant m, E_1(k+1) = E_1(k)$ then m is the minimum embedding dimension. In parallel the mean difference between the raw data $E^*(m)$ is evaluated with respect to m, relating to $\mathcal{N}(m)$ obtained in Eq. (9):

$$E^*(m) = \frac{1}{M}\sum_i |y_p^*(i+mJ) - y_p^*[\mathcal{N}(i,m)+mJ]|. \tag{13}$$

In the same manner as in Eq. (12), the evolution is analyzed through $E_2(m)$:

$$E_2(m) = \frac{E^*(m+1)}{E^*(m)}, \tag{14}$$

and if $\exists k \backslash E_2(k) \neq 1$ then the signal is deterministic; otherwise it is stochastic.

As shown in Fig. 11, the raw signal appears stochastic but the LP filtered one is indeed deterministic, confirming the results obtained with the structure function. The minimum embedding dimension seems to be $m = 19$. It should be noted that a new delay J is computed for the filtered data.

Thus the complete large-scale bimodal dynamics of such a fully turbulent wake are well composed of a stochastic part and a deterministic part as recently proposed in Ref. [30]. In the following sections, we characterize the chaotic behavior of these dynamics through the analysis of the LP filtered signal directly denoted as $y_p^*(t)$.

C. Largest Lyapunov exponent

There are many ways to characterize and quantify chaos. Among the most popular quantities, one can cite the correlation dimension [42], which gives an estimate of the system complexity, and characteristic exponents, which give an estimate of the level of chaos in the dynamical system. In this section, we focus on the Lyapunov exponent. The spectrum of Lyapunov exponents is well known for detecting and quantifying chaotic systems from the experimental time series [43]. Indeed, chaos exists if a system is sensitive to its initial conditions. Thus the principle consists in following the

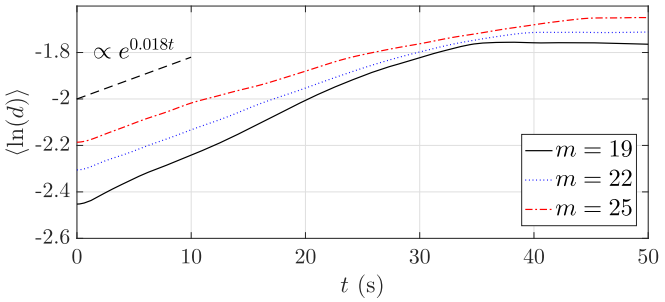

FIG. 12. $\langle \ln(d(t)) \rangle_{i=1..M}$ and exponential approximation $e^{0.018t}$ (black dashed line). $f_p = 100$ Hz.

evolution of the distance d between two initial neighboring state vectors in the phase space. For a chaotic attractor, the distance d exponentially increases in time at an average rate equal to the largest Lyapunov exponent (LLE) λ_1 [44]:

$$d(t) = d(0) \exp^{\lambda_1 t}. \tag{15}$$

We apply Rosenstein's algorithm [45,46], rather than Wolf's algorithm [43], to our LP filtered N-point time series $\{y_p^*(i)\}_{i=1...N}$, due to its efficiency on small data sets. We use the M state vectors $\{Y_i\}_{i=1...M}$ and their closest neighbor $\{Y_{\mathcal{N}(i)}\}_{i=1...M}$ as previously. Then we compute the distance evolution,

$$d_i(j) = \|Y_{i+j} - Y_{\mathcal{N}(i)+j}\|, \tag{16}$$

where $j = [\![f_p t]\!]$ verifies $i + j \leqslant M$ and $\mathcal{N}(i) + j \leqslant M$. The distance $d(t)$ is approximated by averaging over i the distances $d_i(j)$:

$$d(j) = \langle d_i(j) \rangle_i. \tag{17}$$

By taking the logarithm of Eq. (17) with respect to j the slope, extracted through a least-square fit, gives directly the LLE. The distance $d(t)$ computed for our LP filtered data is given in Fig. 12 and it appears to follow Eq. (15) for small t, typically $t \in [0; 1]$ (in second). The LLE is thus computed in this range.

The estimated positive LLE is $\lambda_1 = 0.018 \pm 0.003$ s^{-1}. The relative error is due to the main difficulty of defining the right linear region of the curve to fit. The low-frequency dynamics associated with large-scale structures can thus be considered as a weak chaotic strange attractor.

D. Correlation dimension

The fractal dimension (or Hausdorff dimension) D of a strange attractor can be rigorously approximated by its correlation dimension D_2 which is directly computed from experimental time series according to the works of Ref. [42]. The previous M state vectors $\{Y_i\}_{i=1...M}$ are also used to compute the correlation integral function $\mathcal{C}(\tau)$, defined as

$$\mathcal{C}(\tau) = \frac{2}{M(M-1)} \sum_{i=1}^{M} \sum_{j=i+1}^{M} \Theta(\tau - \|Y_i - Y_j\|), \tag{18}$$

where Θ is the Heaviside function. The correlation dimension D_2 can be derived from the correlation integral function $\mathcal{C}(\tau)$, which scales as a power law for small τ:

$$\mathcal{C}(\tau) \propto \tau^{D_2}, \tag{19}$$

The correlation integral function of our LP filtered signal y_p^* is computed using the Grassberger-Procaccia method improved in Ref. [47], where the authors normalize the Euclidean distance in

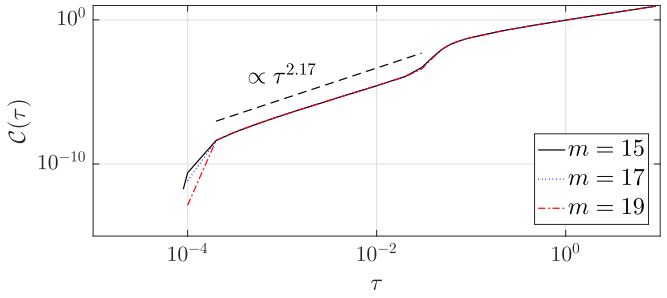

FIG. 13. Correlation integral function $\mathcal{C}(\tau)$ of LP filtered y_p^* and power-law approximation $\propto \tau^{2.17}$ (black dashed line) in logarithmic scale.

Eq. (18) by the embedding dimension m. Figure 13 shows the resulting correlation integral function in logarithmic scale.

Regarding the whole experimental signals we obtain $D_2 = 2.17 \pm 0.01$, which verifies $D_2 \leqslant 2 \log N$ [48]. The correlation dimension is computed over two decades. Furthermore we verify again the low-dimensional aspect of the dynamics using the phase randomization test provided by Ref. [28]: For a stochastic signal the correlation dimension does not change when its Fourier phases are randomized.

Displayed in Fig. 14, the computed correlation dimension after phase randomizing of our signal is clearly different: $D_{2,\text{rand}} = 3.23 \pm 0.01$, which is indicative of chaotic dynamics.

E. Telegraph-like signal

Another interesting way to characterize chaotic oscillator is to analyze the properties of its auto-correlation function (ACF). The ACF of a given function $f(t)$ is defined as $\Gamma_f(\tau) = \langle f(t) f(t+\tau) \rangle_T$, where $\langle . \rangle_T$ stands for the time averaging. The ACF is normalized by $\Gamma_f(0)$. The ACF of a random process has different properties depending on the nature of the system. Among the most popular models used to describe the behavior of many applied random systems, one can cite the noisy harmonic oscillations and the telegraph signal [49]. The model of telegraph signal is particularly well suited to describe the statistics of random switching of a bimodal system in the presence of noise, which is a close description of the bimodal wake. One can distinguish two main kinds of telegraph signals, namely, the random and quasirandom telegraph signals. The random telegraph signal is characterized by a Poisson distribution of switching moments while quasirandom telegraph signal corresponds to random switching between two equiprobable states (probability of switching events equal to $\frac{1}{2}$). For instance, the latter is very well suited to the Lorenz attractor [49].

To characterize our time series as telegraph signals, the first step is then to define two states as the symmetric spanwise positions of the pressure centers as $y^* = \pm y^*_{C_2}$. From our time series, it is

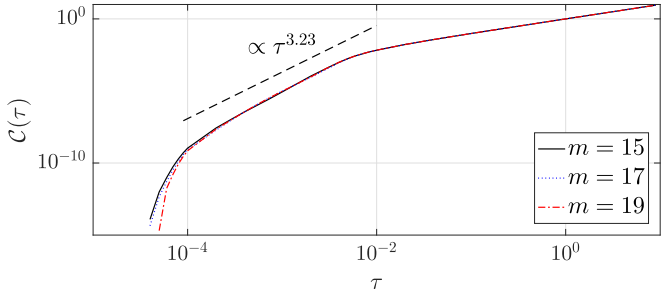

FIG. 14. Correlation integral function $\mathcal{C}(\tau)$ of LP filtered y_p^* after randomizing its Fourier phases and power-law approximation $\propto \tau^{3.23}$ (black dashed line) in logarithmic scale.

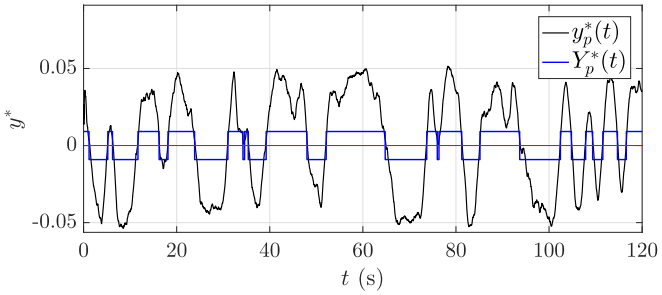

FIG. 15. Part of the telegraph signal $Y_p^*(t)$ (blue) obtained for the pressure barycenter spanwise position $y_p^*(t)$ (black). For clarity the telegraph signal is plotted with a 0.25 factor. Here, $y_{C_2}^* = 3.64\times10^{-2} \pm 1\times10^{-4}$.

then possible to construct a telegraph-like signal Y_p^* such as

$$Y_p^*(t) = \begin{cases} -y_{C_2}^* & \text{if } y_p^*(t) \leqslant 0 \\ y_{C_2}^* & \text{if } y_p^*(t) > 0 \end{cases}. \tag{20}$$

Figure 15 shows a part of the LP filtered signal $y^*(t)$ together with the resulting telegraph signal $Y_p^*(t)$.

The normalized ACF $\Gamma_{y_p^*}(\tau)$ and $\Gamma_{Y_p^*}(\tau)$ are computed for the raw signal and the LP filtered one. According to Ref. [49], the ACF approximation of a random telegraph signal, $\Psi_R(\tau)$, is given by by the following function:

$$\Psi_R(\tau) = e^{-2n_1|\tau|}, \tag{21}$$

where n_1 corresponds to the mean switching frequency, while the ACF of a random telegraph signal can be linearly approximated on short times by the following function $\Psi_{QR}(\tau)$:

$$\Psi_{QR}(\tau) = \begin{cases} 1 - \frac{|\tau|}{\xi_0} & \text{if } |\tau| < \xi_0 \\ 0 & \text{if } |\tau| \geqslant \xi_0 \end{cases}, \tag{22}$$

where ξ_0 corresponds to the minimal residence time in one state, denoted $T_{\min}$. $\Gamma_{y_p^*}(\tau)$, $\Gamma_{Y_p^*}(\tau)$, and the ACF approximations are plotted in Fig. 16.

Figure 16(a) shows that $\Psi_R(n_1 = 0.45)$ is a good approximation of the ACF of the telegraph signal obtained from the raw data. The computed mean switching frequency $n_1 = 0.45$ Hz is close

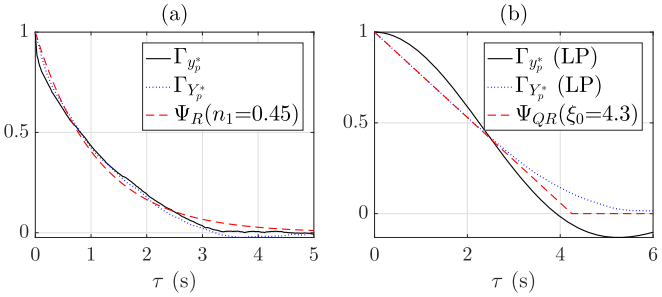

FIG. 16. Normalized autocorrelation functions of the pressure barycenter spanwise position $\Gamma_{y_p^*}$ (black solid line) and of the resulting telegraph-like signal $\Gamma_{Y_p^*}$ (blue dotted line) for (a) the raw signal and (b) the LP filtered one, together with their respective ACF approximations: $\Psi_R(n_1 = 0.45)$ and $\Psi_{QR}(\xi_0 = 4.3)$ (red dashed line).

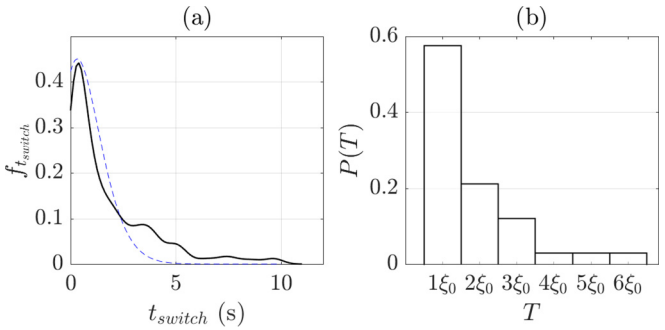

FIG. 17. (a) PDF of the switching time t_{switch} for the raw data (black solid line) together with a Poisson distribution (parameter set to 0.86, blue dashed line) and (b) probabilities of switching at times T multiple to $\xi_0 = 4.3$ for the LP filtered signal.

to the measured one $f_{\text{switch}} = 0.56$ Hz. One can see in Fig. 16(b) that the ACF of the telegraph-like signal extracted from the LP filtered time series is well approximated by the linear function $\Psi_{QR}(\xi_0 = 4.3)$. From the linear approximation we find $\xi_0 = 4.3$ s, which is similar to our filtered experimental results $T_{\text{min}} = 3.6$ s. The same ACF approximation is obtained for the Lorenz attractor described by Eq. (1) [49].

Furthermore, the PDF of the switching times t_{switch} of the raw time series is given in Fig. 17(a), revealing itself close to a Poisson distribution whose parameter is 0.86 s. The mean switching time, which is the parameter of the Poisson distribution, is of the same order as the residential time T_{RSB} seen previously. Regarding the corresponding LP filtered data, the probability of switching $P(T)$ occurring at times T multiple to ξ_0 is computed in Fig. 17(b). The results show that the probability of switching at time $T = \xi_0$ is $P(\xi_0) = 0.56$, agreeing with the ACF approximation of Eq. (22). Reference [49] obtained $P(\xi_0) = 0.52$ for the Lorenz system of Eq. (1), which is also close to 0.5 as expected for such a strange chaotic attractor.

V. CONCLUSIONS AND PERSPECTIVES

The dynamics of the near wake behind a square-back bluff body are characterized by the time evolution of its intensity recirculation barycenter and the spatially averaged rear pressure barycenter. Both quantities track large-scale structures and exhibit strong bimodal distributions characteristic of a random switching process between two states. Their respective spanwise dynamics are highly anticorrelated (phase opposition). Plotting the trajectories of the pressure barycenter over the rear part of the model, similar to a Poincaré section, stochastic behavior is first observed. But applying the same process to the low-frequency signal reveals a chaotic aspect of the dynamics. The instantaneous pressure barycenter circles around two stable areas acting like strange attractors and randomly switches from one attractor to the other. We characterize the chaotic dynamics of these barycenters by reconstructing their phase space and computing the largest Lyapunov exponent and the correlation dimension. All of these elements tend to describe the dynamics of a complex 3D turbulent wake as a weak chaotic system. Apart from its fundamental interest, this result is also of great practical interest. Indeed, if the wake dynamics can be modeled as a chaotic attractor, it opens the path to many closed-loop control strategies which have been first tested on simple chaotic systems such as the Lorenz system [50,51]. Recently, a machine learning control based on the low-pass filtered signal of the rear pressure of the Ahmed body has been successfully performed [52] and a similar one based on the low-frequency dynamics of the wake can be envisioned [53].

ACKNOWLEDGMENT

We deeply acknowledge Diogo Barros, Yacine Bengana, Olivier Cadot, Pierric Joseph, and Laurette Tuckerman for their valuable stimulating discussions.

[1] S. R. Ahmed, G. Ramm, and G. Faltin, *Some salient features of the time-averaged ground vehicle wake*, SAE Technical Paper 840300 (SAE International, 1984).
[2] J.-F. Beaudoin, O. Cadot, J.-L. Aider, K. Gosse, P. Paranthoën, B. Hamelin, M. Tissier, D. Allano, I. Mutabazi, M. Gonzales *et al.*, Cavitation as a complementary tool for automotive aerodynamics, Exp. Fluids **37**, 763 (2004).
[3] M. Grandemange, M. Gohlke, and O. Cadot, Turbulent wake past a three-dimensional blunt body, part 1: Global modes and bi-stability, J. Fluid Mech. **722**, 51 (2013).
[4] J. Östh, B. R. Noack, S. Krajnović, D. Barros, and J. Borée, On the need for a nonlinear subscale turbulence term in POD models as exemplified for a high-Reynolds-number flow over an Ahmed body, J. Fluid Mech. **747**, 518 (2014).
[5] M. Grandemange, O. Cadot, and M. Gohlke, Reflectional symmetry breaking of the separated flow over three-dimensional bluff bodies, Phys. Rev. E **86**, 035302 (2012).
[6] M. Grandemange, M. Gohlke, and O. Cadot, Bi-stability in the turbulent wake past parallelepiped bodies with various aspect ratios and wall effects, Phys. Fluids **25**, 095103 (2013).
[7] O. Cadot, A. Evrard, and L. Pastur, Imperfect supercritical bifurcation in a three-dimensional turbulent wake, Phys. Rev. E **91**, 063005 (2015).
[8] G. Rigas, A. S. Morgans, R. D. Brackston, and J. F. Morrison, Diffusive dynamics and stochastic models of turbulent axisymmetric wakes, J. Fluid Mech. **778**, R2 (2015).
[9] G. Rigas, A. R. Oxlade, A. S. Morgans, and J. F. Morrison, Low-dimensional dynamics of a turbulent axisymmetric wake, J. Fluid Mech. **755**, R5 (2014).
[10] E. N. Lorenz, Deterministic nonperiodic flow, J. Atmos. Sci. **20**, 130 (1963).
[11] P. Achermann, R. Hartmann, A. Gunzinger, W. Guggenbüh, and A. A. Borbély, Correlation dimension of the human sleep electroencephalogram: Cyclic changes in the course of the night, Eur. J. Neurosci. **6**, 497 (1994).
[12] O. Fojt and J. Holcik, Applying nonlinear dynamics to ecg signal processing, IEEE Eng. Med. Biol. Mag. **17**, 96 (1998).
[13] G. Yan, A. De Stefano, E. Matta, and R. Feng, A novel approach to detecting breathing-fatigue cracks based on dynamic characteristics, J. Sound Vib. **332**, 407 (2013).
[14] G. Orlando, A discrete mathematical model for chaotic dynamics in economics: Kaldors model on business cycle, Math. Comput. Simul. **125**, 83 (2016).
[15] T. Matcharashvili, T. Chelidze, Z. Javakhishvili, and E. Ghlonti, Detecting differences in temporal distribution of small earthquakes before and after large events, Comput. Geosci. **28**, 693 (2002).
[16] Y. Eulalie, *Aerodynamic analysis and drag reduction around an Ahmed bluff body*, Ph.D. thesis, Université de Bordeaux, Bordeaux, France, 2014.
[17] F. Champagnat, A. Plyer, G. Le Besnerais, B. Leclaire, S. Davoust, and Y. Le Saint, Fast and accurate PIV computation using highly parallel iterative correlation maximization, Exp. Fluids **50**, 1169 (2011).
[18] N. Gautier and J.-L. Aider, Feed-forward control of a perturbed backward-facing step flow, J. Fluid Mech. **759**, 181 (2014).
[19] N. Gautier and J.-L. Aider, Real-time planar flow velocity measurements using an optical flow algorithm implemented on GPU, J. Vis. **18**, 277 (2015).
[20] N. Gautier and J.-L. Aider, Frequency-lock reactive control of a separated flow enabled by visual sensors, Exp. Fluids **56**, 16 (2015).
[21] C. Pan, D. Xue, Y. Xu, J. Wang, and R. Wei, Evaluating the accuracy performance of Lucas-Kanade algorithm in the circumstance of PIV application, Sci. China Phys. Mech. **58**, 104704 (2015).
[22] D. Barros, *Wake and drag manipulation of a bluff body using fluidic forcing*, Ph.D. thesis, ENSMA, Poitiers, France, 2015.
[23] M. Grandemange, M. Gohlke, V. Parezanović, and O. Cadot, On experimental sensitivity analysis of the turbulent wake from an axisymmetric blunt trailing edge, Phys. Fluids **24**, 035106 (2012).
[24] J. L. Lumley, The structure of inhomogeneous turbulent flows, in *Atmospheric Turbulence and Radio Propagation*, edited by A. M. Yaglom and V. I. Tatarski (Nauka, Moscow, 1967), pp. 166–178.
[25] L. Sirovich, Turbulence and the dynamics of coherent structures, Q. Appl. Math. **45**, 561 (1987).

[26] See Supplemental Material at http://link.aps.org/supplemental/10.1103/PhysRevFluids.2.034604 for short movie following the evolution of the pressure barycenter.
[27] A. R. Osborne and A. Provenzale, Finite correlation dimension for stochastic systems with power-law spectra, Phys. D (Amsterdam, Neth.) **35**, 357 (1989).
[28] A. Provenzale, L. A. Smith, R. Vio, and G. Murante, Distinguishing between low-dimensional dynamics and randomness in measured time series, Physica D **58**, 31 (1992).
[29] B. Mandelbrot, *The Fractal Geometry of Nature* (Henry Holt and Company, New York, 1982).
[30] R. D. Brackston, J. M. García de la Cruz, A. Wynn, G. Rigas, and J. F. Morrison, Stochastic modeling and feedback control of bistability in a turbulent bluff body wake, J. Fluid Mech. **802**, 726 (2016).
[31] J.-P. Eckmann and D. Ruelle, Ergodic theory of chaos and strange attractors, Rev. Mod. Phys. **57**, 617 (1985).
[32] T. Sauer, J. A. Yorke, and M. Casdagli, Embedology, J. Stat. Phys. **65**, 579 (1991).
[33] F. Takens, Detecting strange attractors in turbulence, in *Dynamical Systems and Turbulence, Warwick 1980: Proceedings of a Symposium Held at the University of Warwick 1979/80*, edited by D. Rand and L.-S. Young (Springer, Berlin, 1981), pp. 366–381.
[34] A. M. Fraser and H. L. Swinney, Independent coordinates for strange attractors from mutual information, Phys. Rev. A **33**, 1134 (1986).
[35] B. W. Silverman, Density estimation for statistics and data analysis, in *Monographs on Statistics and Applied Probability* (Chapman and Hall, London, 1986).
[36] R. D. Thomas, N. C. Moses, E. A. Semple, and A. J. Strang, An efficient algorithm for the computation of average mutual information: Validation and implementation in Matlab, J. Math. Psychol. **61**, 45 (2014).
[37] M. Casdagli, S. Eubank, J. D. Farmer, and J. Gibson, State space reconstruction in the presence of noise, Phys. D (Amsterdam, Neth.) **51**, 52 (1991).
[38] L. Cao, Practical method for determining the minimum embedding dimension of a scalar time series, Phys. D (Amsterdam, Neth.) **110**, 43 (1997).
[39] M. B. Kennel, R. Brown, and H. D. I. Abarbanel, Determining embedding dimension for phase-space reconstruction using a geometrical construction, Phys. Rev. A **45**, 3403 (1992).
[40] C. J. Cellucci, A. M. Albano, and P. E. Rapp, Statistical validation of mutual information calculations: Comparison of alternative numerical algorithms, Phys. Rev. E **71**, 066208 (2005).
[41] A.-H. Jiang, X.-C. Huang, Z.-H. Zhang, J. Li, Z.-Y. Zhang, and H.-X. Hua, Mutual information algorithms, Mech. Syst. Signal Process. **24**, 2947 (2010).
[42] P. Grassberger and I. Procaccia, Characteriztion of Strange Attractors, Phys. Rev. Lett. **50**, 346 (1983).
[43] A. Wolf, J. B. Swift, H. L. Swinney, and J. A. Vastano, Determining Lyapunov exponents from a time series, Phys. D (Amsterdam, Neth.) **16**, 285 (1985).
[44] J.-P. Eckmann and D. Ruelle, Ergodic theory of chaos and strange attractors, in *The Theory of Chaotic Attractors*, edited by B. R. Hunt, T.-Y. Li, J. A. Kennedy, and H. E. Nusse (Springer, New York, 2004), pp. 273–312.
[45] M. T. Rosenstein, J. J. Collins, and C. J. De Luca, A practical method for calculating largest Lyapunov exponents from small data sets, Phys. D (Amsterdam, Neth.) **65**, 117 (1992).
[46] S. Sato, M. Sano, and Y. Sawada, Practical methods of measuring the generalized dimension and the largest Lyapunov exponent in high dimensional chaotic systems, Prog. Theor. Phys. **77**, 1 (1987).
[47] T. Ning, J. V. Tranquillo, A. C. Grare, and A. Saraf, Computing correlation integral with the Euclidean distance normalized by the embedding dimension, in *Proceedings of the 2008 9th International Conference on Signal Processing, Beijing, China* (IEEE, Piscataway, NJ, 2008), pp. 2708–2712.
[48] D. Ruelle, The Claude Bernard Lecture, 1989. Deterministic chaos: The science and the fiction, Proc. R. Soc. London, Ser. A **427**, 241 (1990).
[49] V. S. Anishchenko, T. E. Vadivasova, G. A. Okrokvertskhov, and G. I. Strelkova, Correlation analysis of dynamical chaos, Physica A **325**, 199 (2002).
[50] E. Kaiser, B. R. Noack, L. Cordier, A. Spohn, M. Segond, M. Abel, G. Davillier, J. Östh, S. Krajnović, and R. K. Niven, Cluster-based reduced-order modeling of a mixing layer, J. Fluid Mech. **754**, 365 (2014).

[51] F. Guéniat, L. Mathelin, and M. Y. Hussaini, A statistical learning strategy for closed-loop control of fluid flows, Theor. Comput. Fluid Dyn. **30**, 497 (2016).
[52] R. Li, D. Barros, J. Borée, O. Cadot, B. R. Noack, and L. Cordier, Feedback control of bimodal wake dynamics, Exp. Fluids **57**, 158 (2016).
[53] N. Gautier, J.-L. Aider, T. Duriez, B. R. Noack, M. Segond, and M. Abel, Closed-loop separation control using machine learning, J. Fluid Mech. **770**, 442 (2015).